Synthesis of Ni(OH)$_2$-RGO pseudocomposite on nickel foam for supercapacitors with superior performance

Shudi Min[ab], Chongjun Zhao*[a], Zhuomin Zhang[a], Guorong Chen[a], Xiuzhen Qian[a], Zaiping Guo*[b]

[a]*Key Laboratory for Ultrafine Materials of Ministry of Education, Shanghai Key Laboratory of Advanced Polymeric Materials, School of Materials Science and Engineering, East China University of Science and Technology, Shanghai 200237, P.R. China. Tel: +86-21-6425 0838; Fax: +86-21-6425 0838; E-mail: chongjunzhao@ecust.edu.cn*

[b]*Institute for Superconducting and Electronic Materials, University of Wollongong, Wollongong, NSW 2522, Australia. Tel: 61 2 4221 5731; Fax: 61 2 4221 5731; E-mail: zguo@uow.edu.au*

Abstract

A unique structure consisting of two kinds of $Ni(OH)_2$ layers on the top and the bottom, respectively, of the same reduced graphene oxide (RGO) layer has been designed and synthesized through a facile hydrothermal process. The lower layer of $Ni(OH)_2$, covered with a thin RGO film, is transformed in-situ from the surface of a Ni foam substrate through the redox reaction of elemental Ni and graphene oxide (GO), while the upper layer of $Ni(OH)_2$ nanoflakes from Ni ions in the solution is vertically assembled on the top surface of the RGO of the lower $RGO/Ni(OH)_2$ layer. This composite can be regarded as combining RGO with a "pseudocomposite" of $Ni(OH)_2$ material because the upper and lower $Ni(OH)_2$ layers are different in morphology, particle size, and Ni^{2+} source. The bottom layer mainly acts as a rough support, while the upper $Ni(OH)_2$ is suitable to act as the main active material for supercapacitor electrodes. The lower layer of $Ni(OH)_2/RGO$, however, plays key roles in forming the aligned structure and in the subsequent cycling stability. The composite film has a high areal mass loading of 4.7 mg cm^{-2}, and superior supercapacitor performance. It features a specific capacitance of up to 15.65 F cm^{-2} (i.e., 3328.7 F g^{-1}) at a current density of 7 mA cm^{-2} (1.5 A g^{-1}) and a capacity retention of 90.6%, even after 5,000 cycles at the high rate of 20 mA cm^{-2} (4.3 A g^{-1}), indicating that it has a promising application as an efficient electrode for high-performance supercapacitors.

Keywords: Pseudocomposite, Nickel hydroxide/Reduced graphene oxide, Nickel foam, Hydrothermal process, Supercapacitors

1. Introduction

Supercapacitors have attracted great attention for energy storage because of their high power density, long cycle lifetime, and high reliability [1-3]. Therefore, considerable research efforts have been devoted to the design of advanced electrodes with increased performance metrics for supercapacitors [4-6]. Among the wide range of supercapacitor materials that have been explored so far, $Ni(OH)_2$ is one of the most promising candidates and has been attracting increasing attention over recent decades because of its low-cost, environmentally-friendly nature, well-defined redox behavior, and high redox activity [7, 8]. Some challenges are still obstructing its application as an electrode material, however, and one of the major drawbacks for $Ni(OH)_2$ is its very low electrical conductivity ($\sim 10^{-17}\,S\,cm^{-1}$) [9].

As a general and simple electrode preparation method, as-synthesized $Ni(OH)_2$ powder is mixed with a conductive agent, e.g., acetylene black, carbon black. In order to evenly mix the active materials and the carbon conductive agent, the mixture has to be ground for a long time. Moreover, in the case of electrode materials, especially for supercapacitors which need high current or high current density, small-size or even nanosize particles are usually utilized. Hence, this method is not ideal for nanoscale active materials because these components are at different size scales (nanosize vs. microsize) and their interactions are unsatisfactory. In order to overcome this disadvantage, nanosized $Ni(OH)_2$ particles were decorated on the surfaces of individual units of nanosized conductive materials, e.g., on the surface of graphene nanosheets, and then these hybrid $Ni(OH)_2$/graphene materials are mixed with a

common conductive agent so as to further improve their performance [9, 10]. Obviously, a number of preparation processes, including a grinding process and a coating process, are still necessary [9, 10], which is fussy and time-consuming. In addition, the isolating binder could also affect the rate performance of the electrodes [11]. Therefore, it is necessary to find an alternative method to prepare $Ni(OH)_2$ electrode, in which messy electrode preparation is unnecessary, as is the insulating binder.

As a simple and binder-free method, direct growth of active materials on the conductive substrate (subsequent current collector) has becomes a popular electrode preparation route [12-18]. Due to its high mechanical strength, metal substrates are the favorite substrates, especially when Ni is used as substrate, even if no additional Ni source is needed [12]. A pure $Ni(OH)_2$ film can only be used in very thin form, because the performance of dense $Ni(OH)_2$ is limited by its conductivity when the film thickness increases [19]. It appears to be more difficult, however, to increase the conductivity of the film in these direct growth methods, because a conductive agent cannot be simply added, as with the mechanical mixing used in the case of powdery active materials [9, 10]. Therefore, it is necessary to find some way to dope the conductive materials into the film. Graphene, due to its high conductivity (26 000 S cm^{-1}) [20] and high specific surface area (2630 m^2 g^{-1}, theoretical value) [21], provides good electron transfer paths and ensures the direct contact of $Ni(OH)_2$ nanoparticles with graphene, i.e., reliable electrical contact. Furthermore, high conductivity with direct and reliable contact facilitates the application of $Ni(OH)_2$ at

high current density in supercapacitors. Some efficient methods have been used to solve these problems, e.g., by using a graphene coating applied by chemical vapor deposition (CVD), with nickel foam (NF) used as the conductive substrate, although the loading amount of active materials is limited [22, 23]. Unfortunately, for practical applications, particularly for large capacitor applications, such as power sources for hybrid vehicles (HEVs) or fuel cell electric vehicles (FCEVs), high metal oxide concentrations in the electrodes and high mass loading of total materials are needed. To meet this demand, more active materials have to be loaded, after considering the following problems: (1) how to load more active materials onto the same area; (2) porous nanostructured $Ni(OH)_2$ or its composite has to be used so that there are short paths for both electron and ion transfer, (3) adhesion of this expanded porous structure must be improved, so as to resist the repeated expansion-contraction changes during charging-discharging processes. Obviously, it is totally necessary to design some special architecture so as to load more active materials without compromising the electrochemical performance, e.g., special capacitance, high rate capability, and cycling stability.

Increasing the loading amount of active materials will increase the volume of the films, as when the area is defined, the height or thickness must be increased. This indicates that when a continuous $Ni(OH)_2$ structure is formed (e.g., a rod), at least two disadvantages or risks will be induced: increase in resistance because of the long electron paths, which limit operation at high current or high current density, and adhesion of the active materials to the substrate is degraded, so that the active

5

materials slowly come off of the substrate and thus decrease the efficiency and special capacitance. In order to reduce the effect of volume (height or thickness), one method is decreasing the pore size, so that some more space can be occupied by active materials [24]; the other efficient and simple method is to construct a film with two or more discrete layers, i.e., the loading amount of materials can be easily doubled because of the increased layer number. At the same time, the resistance of the whole film can be decreased by inserting a conductive layer, which shortens the transfer paths for electrons in the upper $Ni(OH)_2$ (since the electrons of the top layer will be transferred along the middle conductive layer). Due to its excellent conductivity on both sides, it is favorable to utilize graphene [or reduced graphene oxide (RGO)] as this conductive layer, which make it possible to form a double $Ni(OH)_2$ layer structure on each side of the graphene nanosheets. Moreover, it is easy to pave the whole layer, even with a small amount of graphene, because the graphene is very thin. Decreasing the amount of graphene in the composite can increase the concentration of $Ni(OH)_2$ and thus the pseudocapacitance, and on the other hand, the ultrathin graphene layer ensures the free transfer of the electrolyte ions for the lower $Ni(OH)_2$ layer.

Up to now, there have been no reports on designing and synthesizing graphene with double layers of $Ni(OH)_2$, which may be attributed to the difficulty in forming the lower $Ni(OH)_2$/RGO layer on the Ni substrate with strong adhesion at the interface between NF and $Ni(OH)_2$, or $Ni(OH)_2$/RGO, as well as the potential interface between RGO and the upper $Ni(OH)_2$ layer. Fortunately, in previous work, we found that RGO/$Ni(OH)_2$ could be formed *in-situ* on NF through the redox

reaction of NF and graphene oxide (GO), in which the NF surface is transformed into Ni(OH)$_2$ and GO is reduced to RGO [25], so that a strong interaction exists between the two components at the interface. In addition, Ni^{2+} can be easily decorated on GO sheets due to the static electric force, where it reacts into Ni(OH)$_2$/RGO composite [26, 27]. This indicate that it is possible to build the composite of RGO with a double Ni(OH)$_2$ layer.

In this work, we designed and synthesized Ni(OH)$_2$/RGO/Ni(OH)$_2$ composite films on Ni foam through a simple hydrothermal process, in which the upper Ni(OH)$_2$ layer is deposited from Ni^{2+} in solution and mainly act as the active material, while the lower Ni(OH)$_2$ layer is transformed from elemental Ni on the NF surface and acts as an uneven support. In order to acquire a high specific surface area, an ordered aligned structure of Ni(OH)$_2$ nanoflakes standing vertically was formed. RGO plays important roles in both connecting the upper and lower Ni(OH)$_2$ layers and in controlling the alignment of the Ni(OH)$_2$ nanosheets in the upper Ni(OH)$_2$ layer. Because the two Ni(OH)$_2$ layers are different in terms of their Ni^{2+} source, shape, morphology, and structure, they are like composites from different metal oxides or hydroxides rather than being of the same kind, and hence, the structure is termed a "pseudocomposite". The nano-architecture of this electrode is prepared by a facile one-step hydrothermal approach through the redox reaction between the active Ni foam substrate, Ni^{2+}, and GO, to yield the RGO coated Ni(OH)$_2$ layer. In the meantime, the highly porous Ni(OH)$_2$ nanoflake array is vertically packed on the top side of the RGO, leading to the eventual formation of a multilayer diverse structured

$Ni(OH)_2$/RGO/$Ni(OH)_2$ film on Ni foam substrate. This $Ni(OH)_2$-RGO pseudocomposite film has a high specific capacitance of 3328.7 F g^{-1} (1.5 A g^{-1}), an area-normalized capacitance of up to 15.65 F cm^{-2} (mass loading of 4.7 mg cm^{-2}, current density of 7 mA cm^{-2}). In addition, this pseudocomposite can strongly buffer the volume changes from the phase transformation of $Ni(OH)_2$ during charging and discharging, due to the flexible framework constructed of porous and nanosized $Ni(OH)_2$, and soft and high strength graphene, as well as the uneven bottom $Ni(OH)_2$ layer with high adhesion to the NF substrate. Therefore, this pseudocomposite features excellent cycling stability up to 5000 cycles (90.6 % capacity retention, at 20 mA cm^{-2}). This strategy may be expanded to other metal oxides or hydroxides, including Fe_2O_3, Co_3O_4, ZnO, CuO, Cu_2O, TiO_2, and $Co(OH)_2$.

2. Experimental section

2.1. Materials

Pristine graphite powder, hydrogen chloride (HCl, 36.0-38.0wt%), hydrogen peroxide (H_2O_2, 30.0 wt%), sulfuric acid (H_2SO_4, 98.0 wt%), potassium permanganate ($KMnO_4$, 99.5 wt%), phosphorus pentoxide (P_2O_5, 98.0 wt%), potassium persulfate ($K_2S_2O_8$, 99.5 wt%), ethanol (C_2H_5OH, 99.7 wt%), and nickel nitrate hexahydrate ($Ni(NO_3)_2 \cdot 6H_2O$, 98.0 wt%) were purchased from Sinopharm Chemical Reagent Company. Nickel foam was obtained from Alfa Aesar. All chemicals were used as received without any further purification.

2.2. Synthesis of NF supported $Ni(OH)_2$/RGO/$Ni(OH)_2$ composites

GO was synthesized by a modified Hummer's method [25, 28]. The synthesis of Ni(OH)$_2$/RGO/Ni(OH)$_2$ composites was carried out through a hydrothermal process, by immersing the cleaned Ni foam in mixed solution of GO and nickel salt. Typically, GO (30 mg) and Ni(NO$_3$)$_2$·6H$_2$O (1 m mol) were added to deionized water (50 ml) and dispersed in an ultrasonication bath for 30 min. The NF (1 × 2 cm^2) substrate with the bare area of 1 × 1 cm^2 was then immersed in this aqueous solution. The mixture was loaded into a Teflon-lined stainless steel autoclave (100 ml in volume) for hydrothermal reaction at a designated temperature (i.e., 160 °C, 180 °C, 200 °C, 220 °C, and 240 °C, respectively) for 24 h. The final product was washed with water and ethanol in turn, and then dried in a vacuum oven at 80 °C for 12 h. The samples of Ni(OH)$_2$/RGO/Ni(OH)$_2$/NF composites were denoted as NRNN-160, NRNN-180, NRNN-200, NRNN-220, and NRNN-240 according to the hydrothermal treatment temperatures. RGO/Ni(OH)$_2$/NF-200 (RNN) and Ni(OH)$_2$/NF-200 (NN) composites were prepared under identical conditions except that there was no Ni(NO$_3$)$_2$·6H$_2$O or GO involved. RGO/Ni(OH)$_2$ (RN) composite powder was prepared under identical conditions except without NF.

2.3. Characterization

Wide-angle (10°-80°, 40 kV/200 mA) powder X-ray diffraction (XRD) was conducted using an X-ray diffractometer with Cu Kα radiation (λ = 0.15406 nm). Raman spectra were collected on an INVIA Raman microprobe (Renishaw Instruments, England) with 514 nm laser excitation. The X-ray photoelectron spectroscopy (XPS) spectra were collected on an ESCALAB 250Xi (Thermo Fisher,

U.S.A.) instrument. The morphology and elementary composition of the samples were investigated by field-emission scanning electron microscopy (FESEM, Hitachi S-4800), transmission electron microscopy (TEM, JEOL JEM-2100), and energy dispersive spectroscopy (EDS, Bruker, AXS, Quantax 400-30), respectively.

2.4. Electrochemical Measurements

The electrochemical measurements were performed using a standard three-electrode cell in 1 M KOH aqueous solution. The RN composite powder was mixed with acetylene black (AB) and a binder (polyvinylidene difluoride (PVDF, Aldrich)) in a weight ratio of 8: 1: 1 in N-methyl-2-pyrrolidone (NMP), and the slurry was uniformly pasted onto a NF substrate with an area of 1 cm^2 and then dried at 80 ºC in a vacuum oven for 12 h. The other composite samples with an approximate area of 1×1 cm^2 were directly used as working electrodes, while as-received, platinum foil (2×3 cm^2) and a saturated calomel electrode (SCE) served as the counter and reference electrodes, respectively. Cyclic voltammograms (CV), galvanostatic charge/discharge, and electrochemical impedance spectroscopy (EIS) measurements were carried out using an electrochemical workstation (CHI660e, Shanghai). Impedance spectroscopy measurements were performed at open circuit potential, with a sinusoidal signal of 5 mV in the frequency range from 100 kHz to 0.01 Hz. The loading amount of $Ni(OH)_2/RGO/Ni(OH)_2$ (weight of active material) was determined by the weight difference in the above electrode before testing and after ultrasonic treatment [25].

3. Results and discussion

3.1. XRD patterns, Raman spectra, and XPS of RGO/Ni(OH)$_2$ composites

X-ray diffraction (XRD) patterns of RGO powder, RGO/Ni(OH)$_2$ powder (RN), pure NF, Ni(OH)$_2$/NF (NN), RGO/Ni(OH)$_2$/NF (RNN), and Ni(OH)$_2$/RGO/Ni(OH)$_2$/NF (NRNN) composites prepared at 200°C are shown in Fig. 1(a). Three peaks centered at 44.6°, 51.9°, and 76.4° assigned to the (111), (200), and (220) planes of metallic nickel (JCPDS No. 01-1258), respectively [29], are clearly observed in the patterns of NF and all the composite samples containing NF. The diffraction peaks at 19.3°, 33.2°, 38.6°, 52.0°, 59.1°, 62.7°, 70.4°, and 72.6° in the RN, RNN, and NRNN composites can be ascribed to the (001), (100), (101), (102), (110), (111), (103), and (201) crystalline planes of β-phase Ni(OH)$_2$ (JCPDS No. 14-0117), respectively [12, 30]. As a contrast, the diffraction peaks of Ni(OH)$_2$ in the NN composite are obviously weaker, revealing the poor crystallization in the absence of GO [31]. In the cases of NRNN and RNN, the broad peak of RGO at $2\theta = 25°$ is negligible, due to its low content and the strong peaks of NF and Ni(OH)$_2$ [25, 30]. Meanwhile, with the presence of Ni^{2+}, the diffraction peaks of NRNN become stronger than those of RNN, indicating the enhanced crystallization with multiple Ni sources. In addition, Fig. 1(b) shows the XRD patterns of NRNN composites synthesized at 160°C, 180°C, 200°C, 220°C, and 240°C, respectively. The sharpening of peaks in the XRD pattern is closely related to the small size of the Ni(OH)$_2$ nanoflakes, which were proposed to have high electrochemical activity in previous work [32-34].

The Raman spectra of GO, RGO, and the RN, RNN, and NRNN composites are

shown in Fig. 2(a), and the intensity ratio of the D to the G peak (I_D/I_G) is 0.89, 0.95, 0.93, 0.99, and 1.07, respectively. An increased D/G ratio suggests a decrease in the average size of the in-plane sp^2 domains upon reduction, i.e., RGO has a small size and a large quantity of edges, which act as defects and lead to an increased D peak [27, 35]. Compared with the RNN (0.99) composite, a higher I_D/I_G ratio is obtained for the NRNN (1.07) composite, indicating that the RGO was greatly reduced and formed a high level disordered structure during the hydrothermal process in the presence of NF and Ni^{2+}. In addition, the NRNN composite also presents two characteristic Raman peaks at around 515 cm^{-1} (longitudinal optical, LO) and 1126 cm^{-1} (2LO phonon mode), which are attributed to $Ni(OH)_2$ in the NRNN composite [27, 36, 37], as in the RNN and RN composites.

In order to further identify the chemical composition of the NRNN composite, X-ray photoelectron spectroscopy (XPS) was also performed [Fig. 2(b-d)]. The survey spectrum (0-1100 eV) of the NRNN composite mainly shows carbon (C 1s), oxygen (O 1s), and nickel species [Fig. 2(b)]. The C 1s spectrum of NRNN [Fig. 2(c)] can be divided into three peaks at 284.2, 285.2, and 288.7 eV, which are associated with C–C, C–O, and C=O, respectively [27, 38, 39]. The peak intensities of C–O and C=O for the composite are much smaller than those for the pure GO powder, as shown in previous work [25], indicating considerable deoxygenation after hydrothermal treatment, which is consistent with the Raman results. In addition, in Fig. 2(d), two main peaks at 872.8 and 855.2 eV in the Ni 2p XPS spectra are assigned to Ni 2p$_{1/2}$ and Ni 2p$_{3/2}$, respectively, with a spin-energy separation of 17.6 eV. Furthermore, the

satellite peaks (Ni $2p_{1/2}$, satellite: 878.8 eV; Ni $2p_{3/2}$, satellite: 860.8 eV) are also observed, which are associated with the $Ni(OH)_2$ phase and are in accordance with previously reported data [8, 27, 31, 39-41]. These XPS results are well consistent with the XRD and Raman analysis.

3.2. FESEM images, EDS, and TEM of the composites

Fig. 3(a-d) respectively presents field emission scanning electron microscope (FESEM) images of the RN, NN, RNN, and NRNN composites obtained at 200 °C with 24 h heat-treatment. The powder RN composite [Fig. 3(a)] displays a random and uneven distribution due to the aggregated and crumpled RGO nanosheets that result from the hydrothermal process. In contrast to the $Ni(OH)_2$/NF sample synthesized with NF and H_2O [25], the surface of NN [Fig. 3(b)] was covered by hybrid flat $Ni(OH)_2$ flakes from *in-situ* growth on NF and vertical $Ni(OH)_2$ sheets deposited from solution, so that NN shows a diverse structure based on $Ni(OH)_2$ with different features coming from different Ni sources. The RNN composite [Fig. 3(c)] shows ordered and uniformly oriented array structures, which consist of mackerel-scale $Ni(OH)_2$ flakes on the base and a corrugated graphene coating (Fig. S1 in the Supporting Information), so it is apparent that the presence of GO significantly influences the arrangement of the $Ni(OH)_2$ flakes, and facilitates the formation of conductive network structures in the $RGO/Ni(OH)_2$ composite films on Ni foam substrate [25, 26]. Furthermore, the RGO sheets are efficiently and uniformly distributed on the surface of the $Ni(OH)_2$ layer (Fig. S1), providing a large surface

area for depositing the array of vertical Ni(OH)$_2$ sheets coming from Ni^{2+} in the solution, i.e., the NRNN composite [Fig. 3(d)]. During the hydrothermal process, the mackerel-scale Ni(OH)$_2$ flakes are grown *in-situ* on the NF and the RGO covers its surface to form an ordered network structure, while an array of highly porous Ni(OH)$_2$ sheets is vertically packed on the top side of the RGO, eventually forming a multilayer diverse structure, Ni(OH)$_2$/RGO/Ni(OH)$_2$ film on Ni foam substrate. Based on the especially good solubility and negative electrostatic charge of GO [34, 42], highly oriented and uniform growth of the array of vertical Ni(OH)$_2$ sheets can be achieved, as shown in a low magnification SEM image (Fig. S2). A composite of RGO with two kinds of discrete Ni(OH)$_2$ on both sides of the RGO layer is clearly formed, in which the upper and lower Ni(OH)$_2$ layers can be considered together as a pseudocomposite rather than the same material because of their obvious differences in morphology, size, and Ni source. Cross-sectional scanning electron microscope (SEM) images [Fig. S3(a) and (b)] also show that the upper and lower Ni(OH)$_2$ layers are discrete on both sides of the RGO layer, giving direct evidence of the multilayer diverse structure of Ni(OH)$_2$/RGO/Ni(OH)$_2$ films on Ni foam substrate.

Fig. 4 shows FESEM images of NRNN composites synthesized at different temperatures and the corresponding energy dispersive spectroscopy (EDS) mapping of the NRNN-200 composite. It is clear that similarly oriented structures are formed when the samples are prepared at 160 °C, 180 °C, 200 °C, 220 °C, and 240 °C, except that the size of the primary units of the Ni(OH)$_2$ microstructure slightly changes with temperature, which may be caused by change in the crystallinity. At low temperature

[e.g., 160 °C, Fig. 4(a)], the composite displays a few defects, but with the temperature increasing to 180 °C [Fig. 4(b)], the Ni(OH)$_2$ sheets become more uniform and interconnected with each other. When the temperature reaches 200 °C [Fig. 4(c)], a structured array of highly porous and vertical Ni(OH)$_2$ sheets will form. The corresponding EDS mapping of the NRNN-200 composite (hydrothermal treatment at 200 ºC) was performed to further investigate this structure, and Fig. 4(d-g) shows the elemental maps of carbon [Fig. 4(e)], oxygen [Fig. 4(f)], and nickel (Fig. 4g) in the composite, with the overlay image given in Fig. 4(d). These elemental maps indicate the diverse structure of the Ni(OH)$_2$/RGO/Ni(OH)$_2$ films homogeneously coated on the NF surface, which is also confirmed by the corresponding SEM image shown in Fig. 4(c). Further increasing the temperature induces bigger sheets [Fig. 4(h)], however, or even large and soft sheets with disconnected holes [Fig. 4(i)], which hinder the electrolyte access and transport in electrochemical reactions [43].

The transmission electron microscope (TEM) images of the stacked Ni(OH)$_2$ nanoplates with thickness of 20-25 nm in Fig. 5(a) and its inset also enrich the FESEM analysis by revealing the porous network structure of the composite films. The high resolution TEM (HRTEM) image in Fig. 5(b) shows that the calculated lattice spacing of the nanosheets is about 0.23 nm, which is consistent with the (100) plane of β-Ni(OH)$_2$, confirming its crystalline nature in accordance with the XRD results [31]. The selected-area electron diffraction (SAED) pattern [Fig. 5(b) inset] indicates that these Ni(OH)$_2$ nanoplates are highly crystalline. The single-crystalline nanoplates also show more favorable electrochemical characteristics compared to the

less crystalline small nanoparticles, which is believed to facilitate the electrochemical performance [15, 44, 45].

3.3. Mechanism for the formation of NRNN composite

We have proposed a possible formation route to the NRNN composite based on the experimental results and our earlier work [25, 46, 47]. As illustrated in Scheme 1, during the hydrothermal process, Ni on the foam is directly oxidized into $Ni(OH)_2$, and GO is reduced to RGO, which successfully covers the surface of the $Ni(OH)_2$ layer [Fig. 3(c)], Similarly, in this work, an array of highly porous $Ni(OH)_2$ nanoflakes coming from Ni^{2+} in the solution are vertically packed on the top side of the RGO at the same time, eventually forming a multilayer diverse structure, $Ni(OH)_2/RGO/Ni(OH)_2$ film on Ni foam substrate [Fig. 3(d)]. The GO with its good solubility and negative electrostatic charge also makes for uniform anchoring of the $Ni(OH)_2$ array onto the surface of the GO to fabricate a three-dimensional (3D) porous diverse structure [34, 42], which corresponds to the XRD patterns in terms of the comparison of the intensity of diffraction peaks assigned to $Ni(OH)_2$ in the RNN and NRNN composites. Obviously, RGO play a key role in assembling the vertically aligned $Ni(OH)_2$ nanoflakes.

3.4. Electrochemical performances of NRNN composites

The performance of the NRNN composite films as electrode materials in supercapacitors was evaluated using cyclic voltammetry (CV) and

chronopotentiometry. Fig. 6(a) shows the CV curves of the NRNN electrode in a 1 M

KOH aqueous electrolyte at various scan rates ranging from 1 to 100 mV s^{-1}. Almost

all of the CV curves have a pair of redox peaks within the range of -0.1-0.5 V [vs.

saturated calomel electrode (SCE)], suggesting that the specific capacitance of the

NRNN composite is primarily contributed by pseudocapacitive capacitance, based on

the redox mechanism [26]. The anodic peak (positive current density) at around 0.45

V (vs. SCE) is attributed to the oxidation of Ni(OH)$_2$ to NiOOH, while the cathodic

peak (negative current density) at around 0.25 V (vs. SCE) results from the reverse

reduction process. For Ni(OH)$_2$ electrode, the surface Faradaic reactions will proceed

according to the following reaction [25, 26].

$$Ni(OH)_2 + OH^- \longrightarrow NiOOH + H_2O + e^- \qquad (1)$$
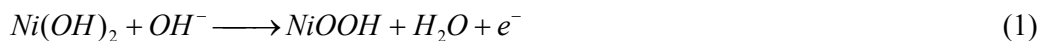
Clearly, all the curves exhibit a similar shape, and the current response increases with

the scan rate. Even at 50 mV s^{-1}, the CV curve still shows a pair of redox peaks,

indicating that this diverse structure is beneficial for fast redox reactions [48].

Fig. 6(b-d) shows the galvanostatic charge/discharge (GCD) performance of the

NRNN composite. The specific capacitance C_s (at a current density of 7 mA cm^{-2},)

can be calculated as in the following equation [48]:

$$C_s = \frac{C}{S} = \frac{I * \Delta t}{\Delta V * S} \qquad (2)$$

where ΔV (V) is the potential window; I (A) is the charge-discharge current; Δt (s) is

the discharge time; and S (cm^2) is the geometric surface area of the NRNN composite

electrode.

Table 1 lists the specific capacitances of the samples prepared at different

temperature. Obviously, it increases firstly in the range from 160 to 200 °C, and then decreases when the temperature increases from 200 °C, through 220 °C, to 240 °C. Therefore, the sample prepared at 200 °C exhibits the best performance (15.65 F cm^{-2}, 3328.7 F g^{-1}), which is much better than that of RGO/Ni(OH)$_2$ composite film [25].

Fig. 6(b) shows the GCD curves at various current densities of 7, 8, 9, 10, 11, 12, 13, 14, 15, and 20 mA cm^{-2} (corresponding to 1.5, 1.7, 1.9, 2.1, 2.3, 2.6, 2.8, 3.0, 3.2, and 4.2 F g^{-1}, respectively), at the potential window from -0.1 V to 0.5 V for the NRNN-200 electrode. The composite electrode retains an areal capacitance of over 7 F cm^{-2}, even at the current density of 20 mA cm^{-2}. This great enhancement in the rate capacitance is contributed by the unique structural features of the composite films. Firstly, the vertically aligned scaffold and porous channels of the Ni(OH)$_2$ nanoflakes make it possible to expose almost all of the surface, providing plentiful electroactive sites for redox reactions [49]. Secondly, the well-defined porous channels between the Ni(OH)$_2$ nanoflakes allow easy access to the electrolyte, which shortens the transfer pathways of ions, i.e., enhances the diffusion kinetics. Thirdly, as the electrolyte has a penetration depth of approximately 20 nm [50, 51], whereas the thickness of the Ni(OH)$_2$ nanoflakes is 20-25 nm [Fig. 5(a) and inset], they can make the active materials almost 100% usable for the redox reaction. Hence, this special architecture of RGO and the double Ni(OH)$_2$ layers facilitates its utilization in supercapacitors, especially at high rates [43, 49].

The areal capacitance and gravimetric capacitance values of the NRNN electrode can be calculated, and the results are plotted in Fig. 6(c). The highest areal

capacitance achieved on the NRNN electrode is 15.65 F cm^{-2} (i.e., 3328.7 F g^{-1}) at 7 mA cm^{-2}. To the best of our knowledge, this value is the highest reported for this kind of composite for supercapacitor electrodes (The highest value for specific capacitance is 3300 F g^{-1} for a Ni(OH)$_2$/CNT/NF electrode) [7].

The long-term cycling performance of this composite electrode is recorded as shown in Fig. 6(d). It can be observed that the specific capacitance increases by about 0.94% during the first 100 cycles, which may be due to electrode activation, which increases the number of available active sites and allows the trapped ions to gradually diffuse out [48, 49, 52]. Importantly, the NRNN composite electrode exhibits superior cycling stability, with a stable capacitance (only 4.7% capacity decay) after 3,000 cycles of charging and discharging at a current density of 20 mA cm^{-2}, this is much better than for the RNN composite electrode (~19.4% capacity decay) under identical test conditions. This superior cycling stability is closely related to the unique morphology and stable structure of the NRNN composite, the comparison of XRD patterns (Fig. S4) and FESEM images [Fig. S5 and Fig. 3(d)] before and after charged and discharged for 3000 cycles also prove that the structure and morphology of NRNN was good kept. Furthermore, it has 90.6% capacity retention even after 5,000 cycles of charging and discharging [Fig. 6(d) inset]. The superior cycling performance is related to this unique diverse structure. The volume changes that accompany the redox reactions of active materials are the main cause of limited cycle life [3], the high porosity of the Ni(OH)$_2$ flakes can provide buffer space for volume changes from the phase transformation of Ni(OH)$_2$ during the charging and discharging [38]. It is

worth noting that the morphology of the Ni(OH)$_2$/RGO with no upper Ni(OH)$_2$ layer contributes to the cycling stability by lessening the shock of volume changes, based on both the soft and highly flexible RGO and the uneven rather than flat Ni(OH)$_2$ surface. For comparison, in the Ni(OH)$_2$ formed on hard solid Ni, the Ni(OH)$_2$ grains flaked off from nickel substrate due to their loose packing, and there was only 48% retention of capacitance after 300 cycles [14].

The performance of the composite electrode was further confirmed by electrochemical impedance spectroscopy (EIS). Fig. 7 presents the Nyquist plots of the NRNN and RNN composite electrodes collected in the frequency range from 100 kHz to 0.01 Hz, with an ac excitation signal of 5 mV. These plots display a semicircle in the high frequency range and a straight line in the low frequency region, which correspond to electron-transfer-limited processes and diffusion-limited electron-transfer processes, respectively [41, 53]. The x-intercept of the plot at high frequency represents the equivalent series resistance (R_s) of the electrodes, and the diameter of the semicircle corresponds to the charge transfer resistance (R_{ct}) at the contact interface between the electrodes and electrolyte solution [41, 54]. As can be seen from the Fig. 7 inset, the NRNN displays a smaller R_s value (1.15 Ω) and R_{ct} value (0.26 Ω) than for the RNN (R_s value: 1.28 Ω, and R_{ct} value: 0.3 Ω). Additionally, the NRNN composite electrode exhibits a line that is closer to vertical in the low frequency region, indicating the good electrochemical capacitance of the NRNN electrode in the KOH aqueous solution [48]. Importantly, the low resistance of the NRNN electrode and the contact resistance between the composite film and NF

substrate are expected to raise the upper limit of the high charge-discharge rate of the supercapacitor [55, 56], which is also thanks to this unique diverse structure with high orientation and uniformity. These results indicate that the NRNN composite exhibits good current rate properties, which is consistent with the CV and GCD results.

4. Conclusion

In summary, we have designed and synthesized a "pseudocomposite" of two $Ni(OH)_2$ layers with different morphologies and the same RGO layer between them through a facile one-step hydrothermal approach. Owing to the favorable structural features, this composite electrode exhibits a superior specific capacitance of up to 15.65 F cm^{-2} (i.e., 3328.7 F g^{-1}) at a current density of 7 mA cm^{-2} (1.5 A g^{-1}) in 1 M KOH solution. In addition, the electrode exhibits excellent cycling stability, with capacity retention of 90.6% after 5,000 cycles. These results demonstrate the importance of the composite's structural design for fabricating electrodes. More importantly, this electrode design concept also can be easily generalized to other metal oxide (or hydroxide, sulfide, phosphide)/RGO composite materials with unique diverse structure for high-performance supercapacitors.

References

[1] P. Simon and Y. Gogotsi, *Nat. Mater.*, 2008, **7**, 845-854.

[2] M. Winter and R.J. Brodd, *Chem. Rev.*, 2004, **104**, 4245-4269.

[3] J.R. Miller and P. Simon, *Science*, 2008, **321**, 651-652.

[4] Y. Hou, Y.W. Cheng, T. Hobson and J. Liu, *Nano Lett.*, 2010, **10**, 2727-2733.

[5] J.H. Zhong, A.L. Wang, G.R. Li, J.W. Wang, Y.N. Ou and Y.X. Tong, *J. Mater. Chem.*, 2012, **22**, 5656-5665.

[6] H.P. Cong, X.C. Ren, P. Wang and S.H. Yu, *Energy Environ. Sci.*, 2013, **6**, 1185-1191.

[7] Z. Tang, C.H. Tang and H. Gong, *Adv. Funct. Mater.*, 2012, **22**, 1272-1278.

[8] F.Q. Zhang, D. Zhu, X. Chen, X. Xu, Z. Yang, C. Zou, K.Q. Yang and S.M. Huang, *Phys. Chem. Chem. Phys.*, 2014, **16,** 4186-4192.

[9] Z.P. Sun and X.M. Lu, *Ind. Eng. Chem. Res.*, 2012, **51**, 9973-9979.

[10] H.J. Yan, J.W. Bai, J. Wang, X.Y. Zhang, B. Wang, Q. Liu and L.H. Liu, *CrystEngComm*, 2013, **15**, 10007-10015.

[11] Y.W. Cheng, H.B. Zhang, C.V. Varanasi and J. Liu, *Energy Environ. Sci.*, 2013, **6**, 3314-3321.

[12] B.L. Hu, X.Y. Qin, A.M. Asiri, K.A. Alamry, A.O. Al-Youbi and X.P. Sun, *Electrochim. Acta*, 2013, **107**, 339-342.

[13] G.X. Hu, C.X. Li and H. Gong, *J. Power Sources*, 2010, **195**, 6977-6981.

[14] G.W. Yang, C.L. Xu and H.L. Li, *Chem. Commun.*, 2008, **48**, 6537-6539.

[15] J.T. Li, W. Zhao, F.Q. Huang, A. Manivannan and N.Q. Wu, *Nanoscale*, 2011, **3**,

5103-5109.

[16] U.M. Patil, K.V. Gurav, J.H. Kim, C.D. Lokhande and S.C. Jun, *Bull. Mater. Sci.*, 2014, **37**, 27-33.

[17] J.Y. Ji, L.L. Zhang, H.X. Ji, Y. Li, X. Zhao, X. Bai, X.B. Fan, F.B. Zhang and R.S. Ruoff, *ACS Nano*, 2013, **7**, 6237-6243.

[18] G.S. Gund, D.P. Dubal, S.B. Jambure, S.S. Shinde and C.D. Lokhande, *J. Mater. Chem. A*, 2013, **1**, 4793-4803.

[19] Z.Y. Lu, Z. Chang, W. Zhu and X.M. Sun, *Chem. Commun.*, 2011, **47**, 9651-9653.

[20] C.H. Park, F. Giustino, C.D. Spataru, M.L. Cohen and S.G. Louie, *Nano Lett.*, 2009, **9**, 4234-4239.

[21] M.D. Stoller, S.J. Park, Y.W. Zhu, J.H. An and R.S. Ruoff, *Nano Lett.*, 2008, **8**, 3498-3502.

[22] T. Xiao, X. Hu, B. Heng, X. Chen, W. Huang, W. Tao, H. Wang, Y. Tang, X. Tan and X. Huang, *J. Alloys Compd.*, 2013, **549**, 147-151.

[23] X. Wang, J.Y. Liu, Y.Y. Wang, C.M. Zhao and W.T. Zheng, *Mater. Res. Bull.*, 2014, **52**, 89-95.

[24] J. Chmiola, G. Yushin, Y. Gogotsi, C. Portet, P. Simon and P.L. Taberna, *Science*, 2006, **313**, 1760-1763.

[25] S.D. Min, C.J. Zhao, G.R. Chen and X.Z. Qian, *Electrochim. Acta*, 2014, **115**, 155-164.

[26] H.L. Wang, H.S. Casalongue, Y.Y. Liang and H.J. Dai, *J. Am. Chem. Soc.*, 2010, **132**, 7472-7477.

[27] J. Yan, W. Sun, T. Wei, Q. Zhang, Z.J. Fan and F. Wei, *J. Mater. Chem.*, 2012, **22**, 11494-11502.

[28] W.S. Hummers and R.E. Offeman, *J. Am. Chem. Soc.*, 1958, **80**, 1339-1339.

[29] A. Lamberti, M. Destro, S. Bianco, M. Quaglio, A. Chiodoni, C.F. Pirri and C. Gerbaldi, *Electrochim. Acta*, 2012, **86**, 323-329.

[30] D.L. Fang, Z.D. Chen, X. Liu, Z.F. Wu and C.H. Zheng, *Electrochim. Acta*, 2012, **81**, 321-329.

[31] Z. Wu, X.L. Huang, Z.L. Wang, J.J. Xu, H.G. Wang and X.B. Zhang, *Scientific Reports Sci. Rep.*, 2014, **4**, 3669/1-3669/8.

[32] X. Sun, G.K. Wang, J.Y. Hwang and J. Lian, *J. Mater. Chem.*, 2011, **21**, 16581-16588.

[33] D.P. Dubal, G.S. Gund, C.D. Lokhande and R. Holze, *ACS Appl. Mater. Interfaces*, 2013, **5**, 2446-2454.

[34] L.Q. Wang, X.C. Li, T.M. Guo, X.B. Yan and B.K. Tay, *Int. J. Hydrogen Energy*, 2014, **39**, 7876-7884.

[35] S.Z. Zu and B.H. Han, *J. Phys. Chem. C*, 2009, **113**, 13651-13657.

[36] W.J. Zhou, X.H. Cao, Z.Y. Zeng, W.H. Shi, Y.Y. Zhu, Q.Y. Yan, H. Liu, J.Y. Wang and H. Zhang, *Energy Environ. Sci.*, 2013, **6**, 2216-2221.

[37] C.H. Jiang, B.B. Zhan, C. Li, W. Huang and X.C. Dong, *RSC Adv.*, 2014, **4**, 18080-18085.

[38] J.W. Lee, T. Ahn, D. Soundararajan, J.M. Ko and J.D. Kim, *Chem. Commun.*, 2011, **47**, 6305-6307.

[39] J. Yan, Z.J. Fan, W. Sun, G.Q. Ning, T. Wei, Q. Zhang, R.F. Zhang, L.J. Zhi and F. Wei, *Adv. Funct. Mater.*, 2012, **22**, 2632-2641.

[40] L. Jiang, R.J. Zou, W.Y. Li, J.Q. Sun, X.H. Hu, Y.F. Xue, G.J. He and J.Q. Hu, *J. Mater. Chem. A*, 2013, **1**, 478-481.

[41] X. Chen, X.H. Chen, F.Q. Zhang, Z. Yang and S.M. Huang, *J. Power Sources*, 2013, **243**, 555-561.

[42] J.T. Zhang, S. Liu, G.L. Pan, G.R. Li and X.P. Gao, *J. Mater. Chem. A*, 2014, **2**, 1524-1529.

[43] H. Chen, L.F. Hu, Y. Yan, R.C. Che, M. Chen and L.M. Wu, *Adv. Energy Mater.*, 2013, **3**, 1636-1646.

[44] Y.X. Xu, X.Q. Huang, Z.Y. Lin, X. Zhong, Y. Huang and X.F. Duan, *Nano Res.*, 2013, **6**, 65-76.

[45] G.Q. Zhang, H.B. Wu, H.E. Hoster, M.B.C. Park and X.W. Lou, *Energy Environ. Sci.*, 2012, **5**, 9453-9456.

[46] S.D. Min, C.J. Zhao, G.R. Chen, Z.M. Zhang and X.Z. Qian, *Electrochim. Acta*, 2014, **135**, 336-344.

[47] C. J. Zhao, S.L. Chou, Y.X. Wang, C.F. Zhou, H.K. Liu and S.X. Dou, *RSC Adv.*, 2013, **3**, 16597-16603.

[48] C.Z. Yuan, J.Y. Li, L.R. Hou, X.G. Zhang, L.F. Shen and X.W. Lou, *Adv. Funct. Mater.*, 2012, **22**, 4592-4597.

[49] X.J. Zhang, W.H. Shi, J.X. Zhu, W.Y. Zhao, J. Ma, S. Mhaisalkar, T.L. Maria, Y.H. Yang, H. Zhang, H.H. Hng and Q.Y. Yan, *Nano Res.*, 2010, **3**, 643-652.

[50] C.C. Hu, K.H. Chang, M.C. Lin and Y.T. Wu, *Nano Lett.*, 2006, **6**, 2690-2695.

[51] H.M. Du, L.F. Jiao, K.Z. Cao, Y.J. Wang and H.T. Yuan, *ACS Appl. Mater. Interfaces*, 2013, **5**, 6643-6648.

[52] C.Z. Yuan, X.G. Zhang, L.H. Su, B. Gao and L.F. Shen, *J. Mater. Chem.*, 2009, **19**, 5772-5777.

[53] T. Zhai, F.X. Wang, M.H. Yu, S.L. Xie, C.L. Liang, C. Li, F.M. Xiao, R.H. Tang, Q.X. Wu, X.H. Lu and Y.X. Tong, *Nanoscale*, 2013, **5**, 6790-6796.

[54] S. Biswas and L.T. Drzal, *Chem. Mater.*, 2010, **22**, 5667-5671.

[55] H.T. Zhang, X. Zhang, D.C. Zhang, X.Z. Sun, H. Lin, C.H. Wang and Y.W. Ma, *J. Phys. Chem. B*, 2013, **117**, 1616-1627.

[56] A. Burke, *J. Power Sources*, 2000, **91**, 37-50.

Figure Captions

Fig. 1. XRD patterns of (a) pure RGO powder, RGO/Ni(OH)$_2$ powder (RN), NF, Ni(OH)$_2$/NF (NN), RGO/Ni(OH)$_2$/NF (RNN), and Ni(OH)$_2$/RGO/Ni(OH)$_2$/NF (NRNN) composites; (b) NRNN composites prepared at 160, 180, 200, 220, and 240°C.

Fig. 2. (a) Raman spectra of GO, pure RGO obtained hydrothermally at 200°C, RN, RNN, and NRNN. (b)-(d) XPS spectra of NRNN composite: (b) survey spectrum, (c) C 1s spectrum, and (d) Ni 2p spectrum of the NRNN composite.

Fig. 3. FESEM images of (a) RGO/Ni(OH)$_2$ (RN) powder composite, (b) Ni(OH)$_2$/NF (NN) composite, (c) RGO/Ni(OH)$_2$/NF (RNN) composite, and (d) Ni(OH)$_2$/RGO/Ni(OH)$_2$/NF (NRNN) composite.

Fig. 4. FESEM images of (a) NRNN-160, (b) NRNN-180, (c) NRNN-200. (d-g) EDS mapping of the NRNN-200 composite: (d) overlay of C, O, and Ni elements, (e) C element (red), (f) O element (blue), and (g) Ni element (green). (h) NRNN-220, and (i) NRNN-240.

Fig. 5. (a) TEM image and corresponding magnified TEM image (inset) of the NRNN-200 composite; (b) HRTEM image and SAED pattern (inset) of the NRNN-200 composite.

Fig. 6. (a) Cyclic voltammograms (CV) of NRNN electrode at various scan rates; (b) galvanostatic charge/discharge (GCD) curves of NRNN electrode at various current densities; (c) current dependence of the area capacitance (lower curve) and specific capacitance (upper curve) of the NRNN electrode; and (d) cycling

performance of the NRNN and RNN electrodes at a current density of 20 mA

cm^{-2}. The inset is the 5,000 cycle curve of NRNN at a current density of 20 mA

cm^{-2}.

Fig. 7. EIS spectra of NRNN and RNN composite electrodes in the frequency range

from 100 kHz to 0.01 Hz. The inset is the enlarged plot in the high frequency

region.

Scheme

Scheme 1. Schematic representation of the formation process of the

RGO/Ni(OH)$_2$/NF (RNN) and Ni(OH)$_2$/RGO/Ni(OH)$_2$/NF (NRNN) composites.

Tables

Table 1. Specific capacitance, areal and gravimetric of RN-200, NN-200, RNN-200,

and NRNN-160, 180, 200, 220, and 240 composite electrodes at a current

density of 7 mA cm^{-2}.

Table 1

Samples	Areal capacitance (F cm^{-2})	Active material loading (mg)	Gravimetric capacitance (F g^{-1})
RN-200	2.18	1.5	1454.4
NN-200	0.35	0.4	875
RNN-200	2.78	1.8	1542.6
NRNN-160	11.89	4.4	2701.9
NRNN-180	14.35	4.5	3188.9
NRNN-200	15.65	4.7	3328.7
NRNN-220	13.72	4.4	3118.2
NRNN-240	9.23	4.5	2050.7
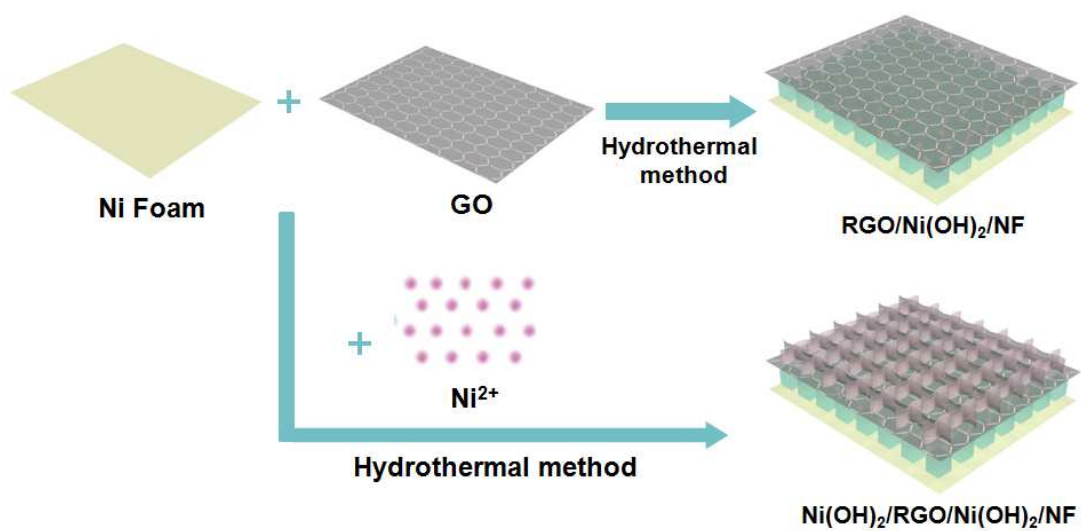
Scheme 1
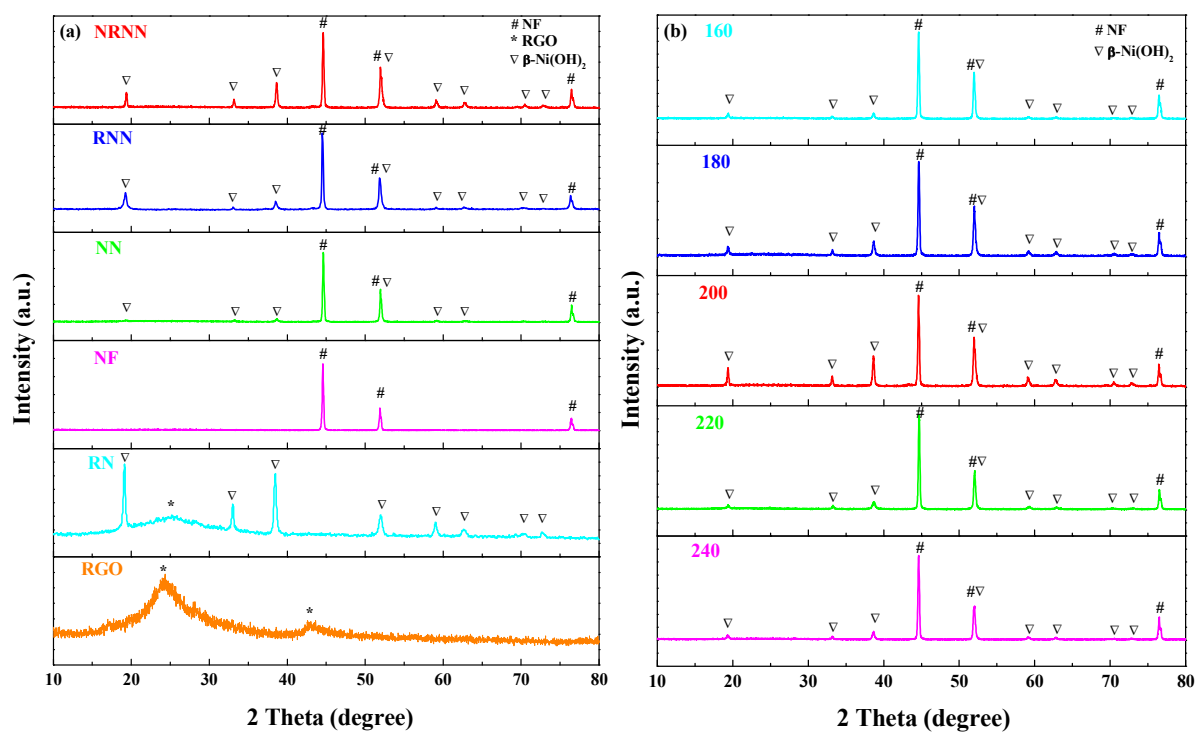
Fig. 1
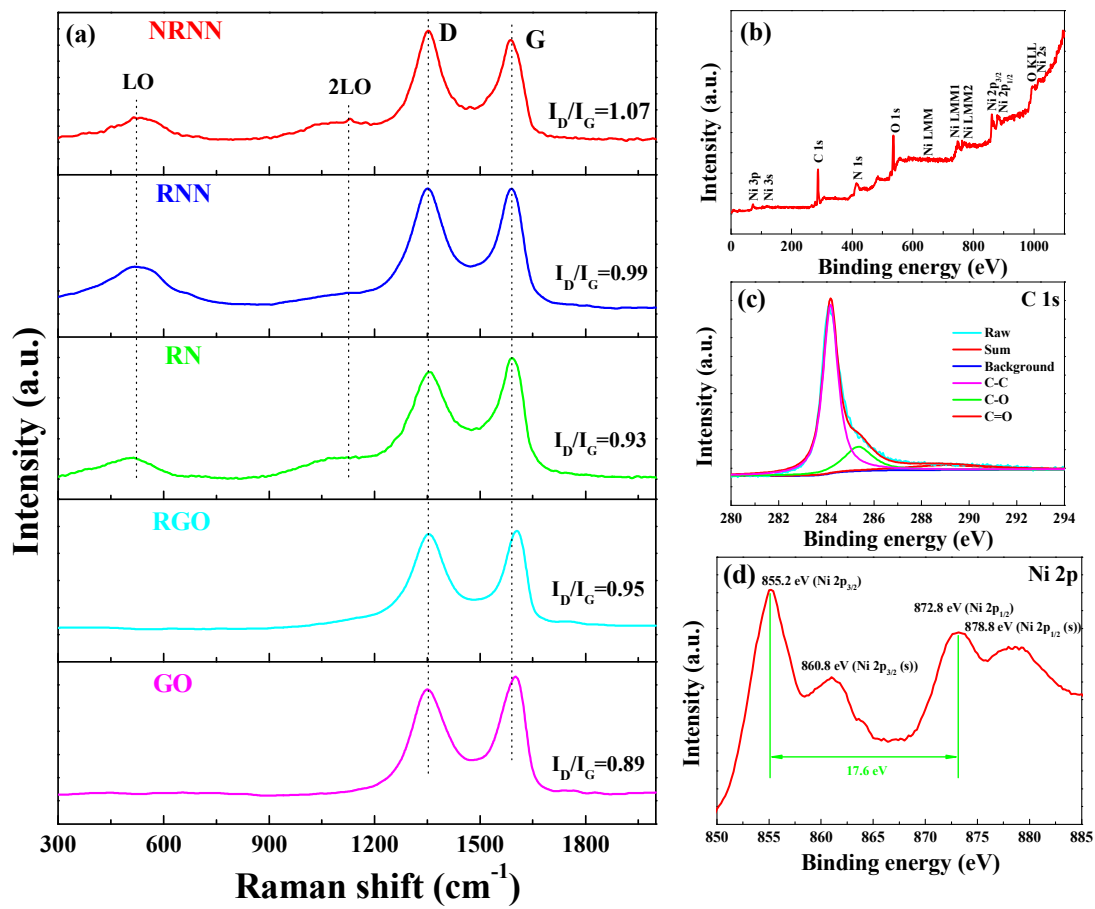
Fig. 2
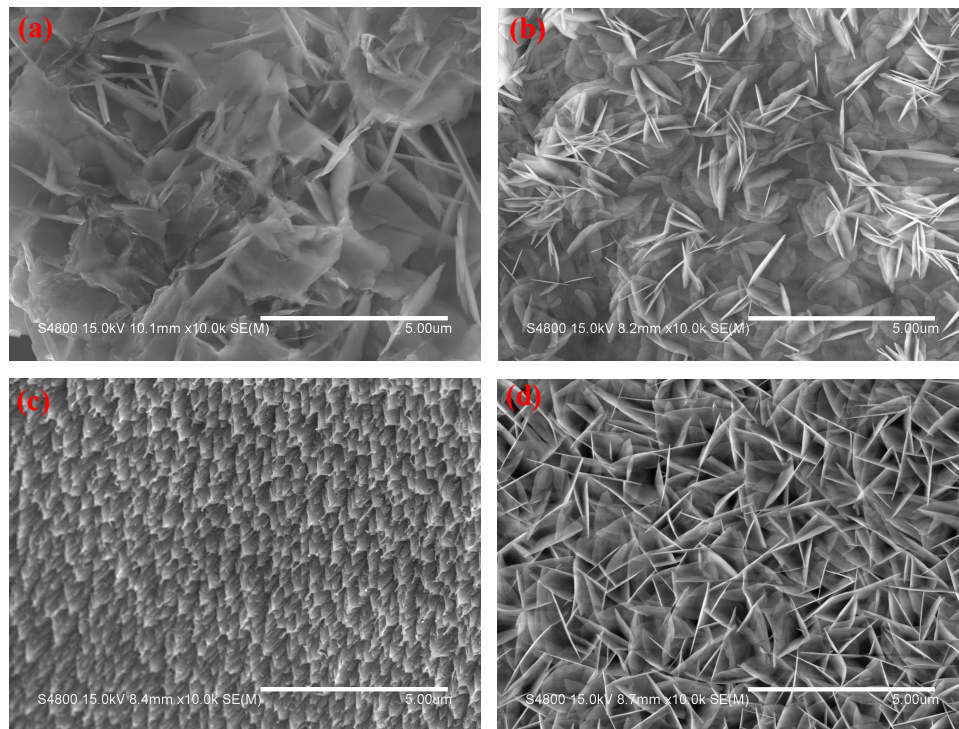
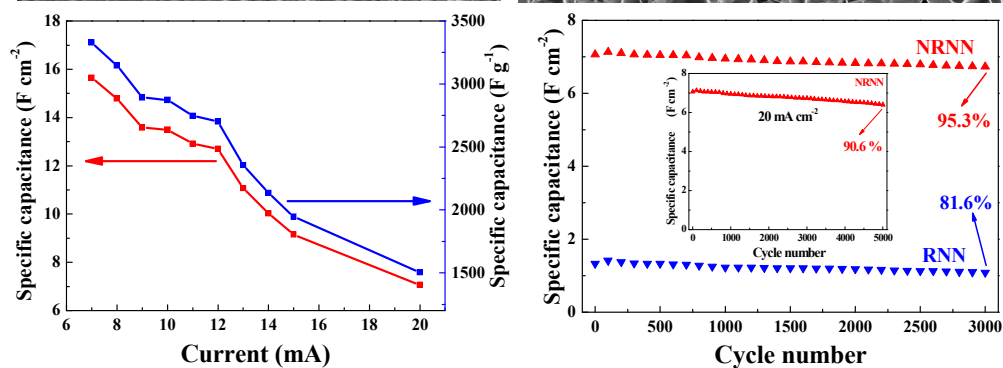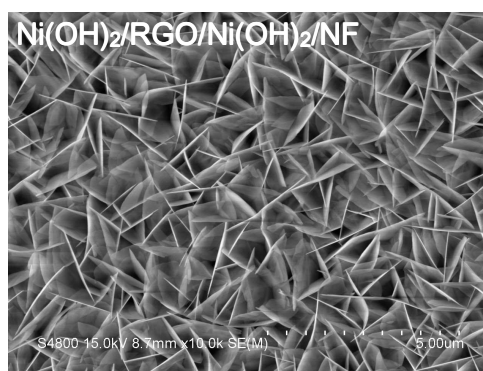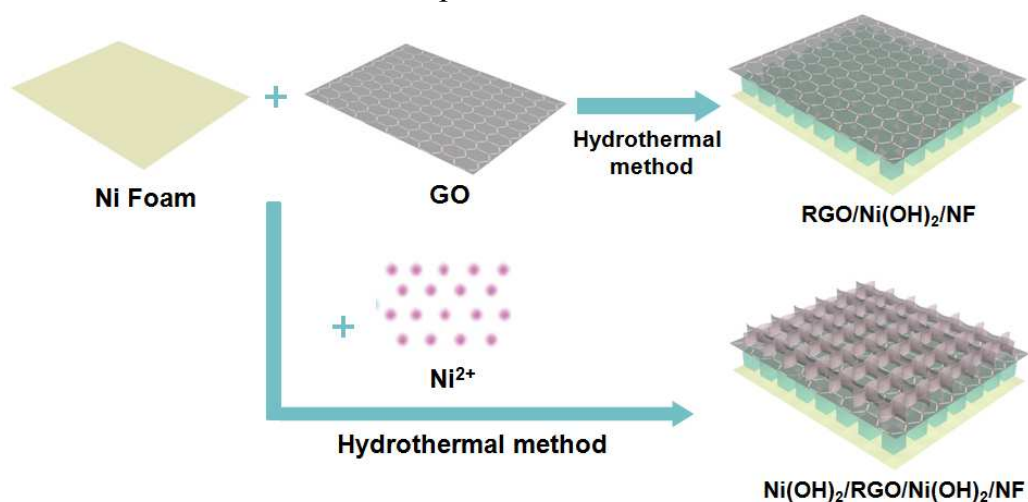**Fig . 3**
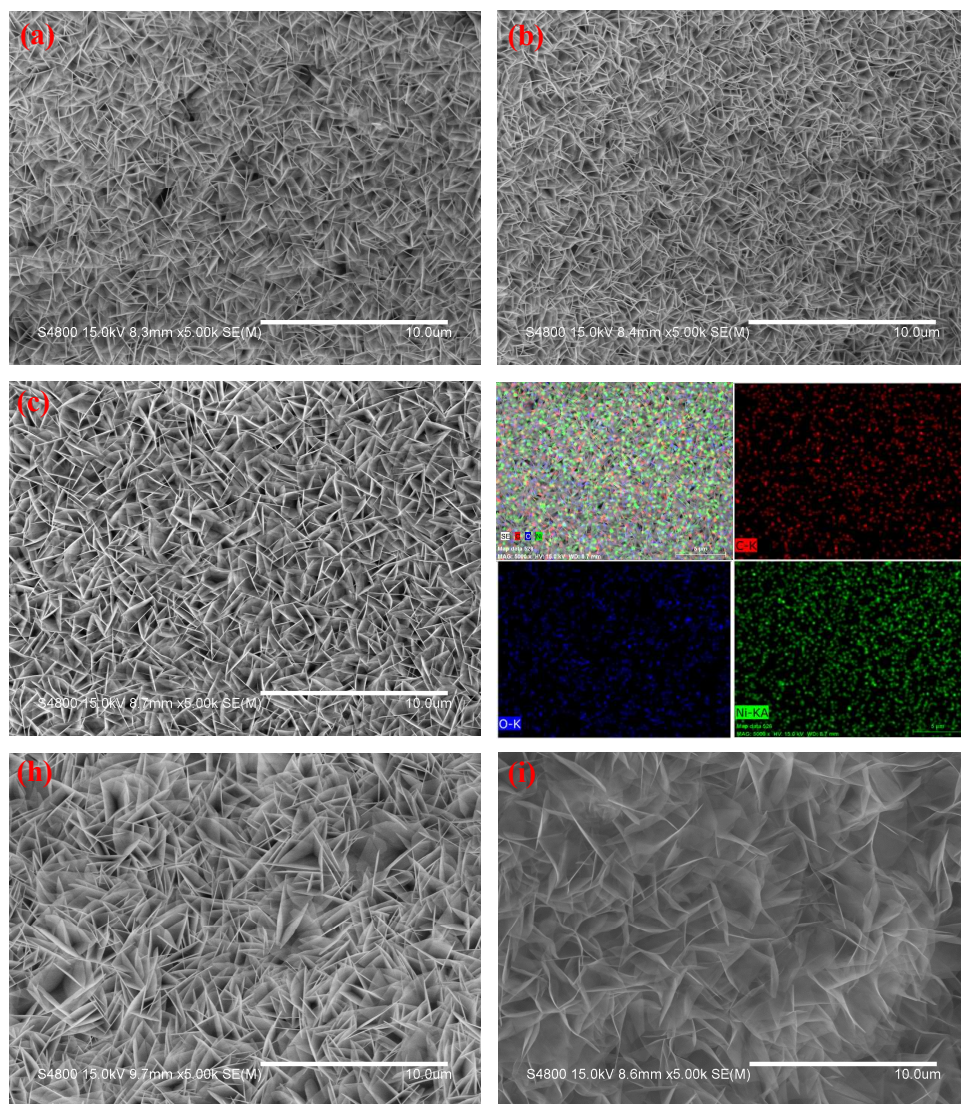
Fig. 4
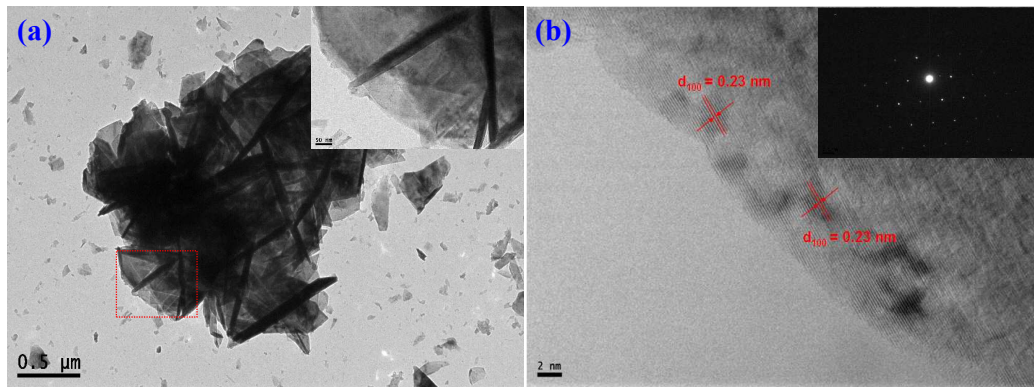
Fig. 5
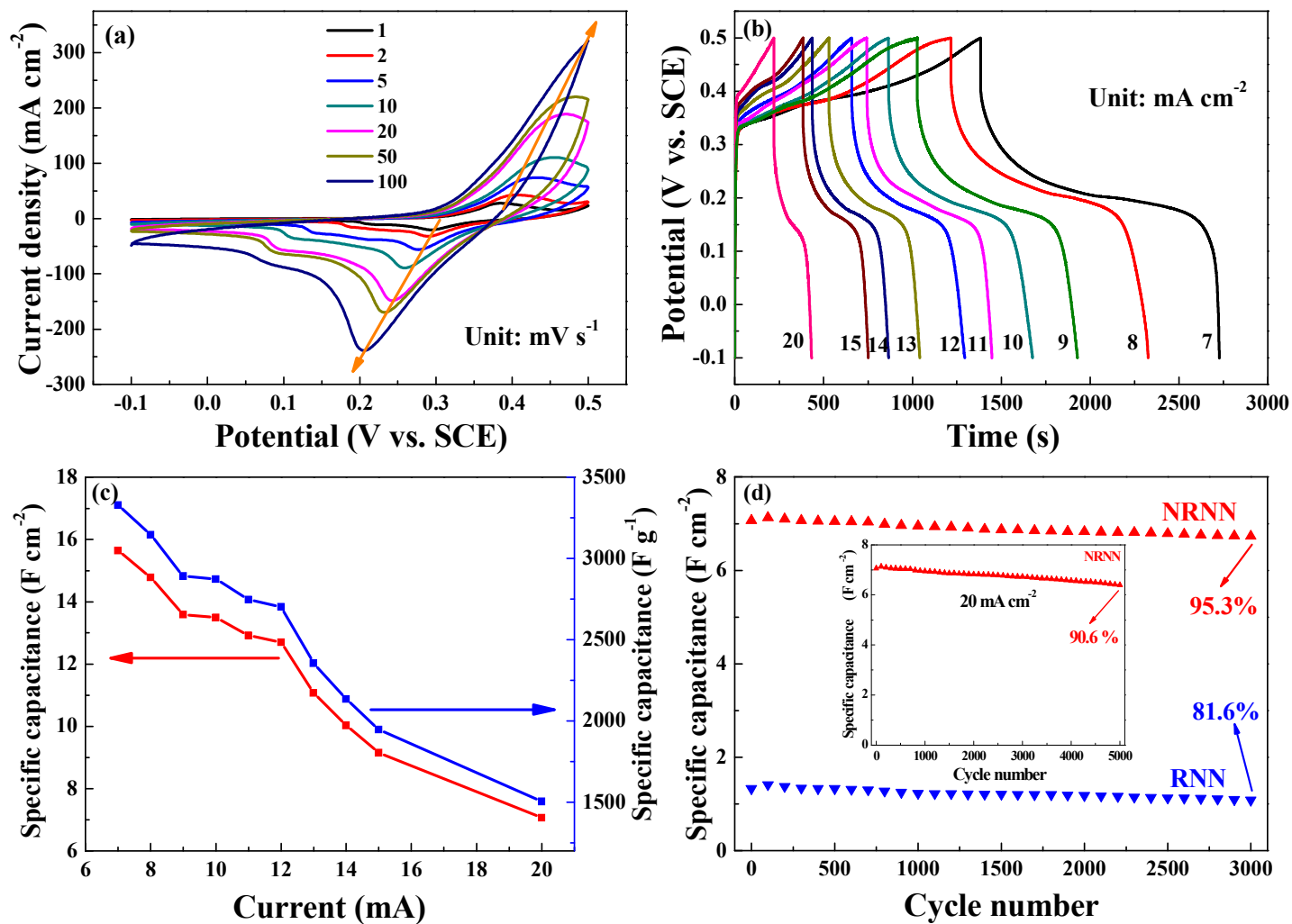
Fig. 6
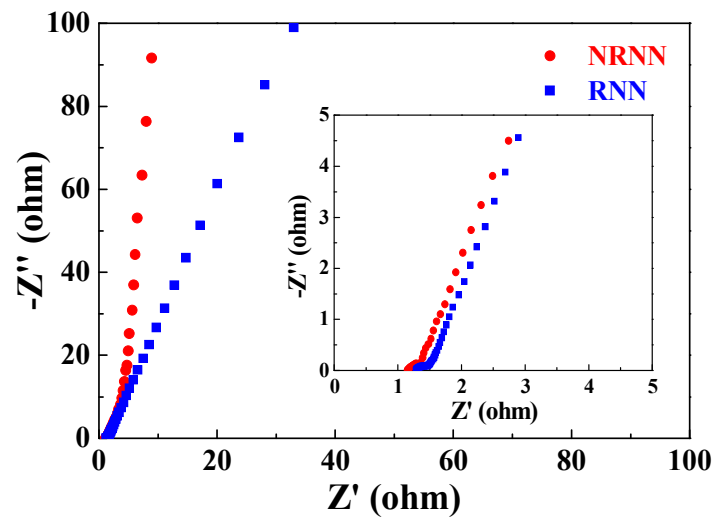
Fig. 7

Graphical Abstract

A "pseudocomposite" with unique nano-architecture of two $Ni(OH)_2$-RGO layer with the same RGO veneer was designed and *in-situ* synthesized on nickel foam (NF) using a facile one-pot hydrothermal approach, which exhibits superior capacitive performance (15.65 F cm^{-2} at 7 mA cm^{-2}, i.e., 3328.7 F g^{-1} at 1.5 A g^{-1}, and 90.6 % capacity retention after 5000 cycles at 20 mA cm^{-2}).